JOURNAL OF CATALYSIS **169,** 327–337 (1997)
ARTICLE NO. CA971711

Alkali–Support Interactions on Rubidium Base Catalysts Determined by XANES, EXAFS, CO_2 Adsorption, and IR Spectroscopy

E. J. Doskocil, S. V. Bordawekar, and R. J. Davis[1]

Department of Chemical Engineering, University of Virginia, Charlottesville, Virginia 22903-2442

Received January 7, 1997; revised March 26, 1997; accepted March 31, 1997

Rubidium was supported on a variety of carriers, including magnesia, titania, alumina, carbon, and silica, by decomposition of an impregnated acetate precursor at 773 K. Except for Rb/MgO, none of the oxide-based samples contained surface carbonates as detected by IR spectroscopy after pretreatment at 773 K. The XANES and EXAFS associated with the Rb *K* edge indicated that the local structure around Rb was highly dependent on the support composition. For example, the Rb–O distance was significantly shorter on carbon and silica compared to more basic carriers. Results from CO_2 stepwise TPD showed that Rb/MgO possessed strongly basic sites that were not present on pure MgO. The basic sites formed by Rb addition to the other supports were weaker than those on Rb/MgO. Decomposition of 2-propanol at 593 K was used to relate catalytic activity to surface basicity. As anticipated, Rb/MgO and MgO were highly active and selective for alcohol dehydrogenation. Addition of Rb to alumina and titania greatly decreased the activity of the support oxides for the acid-catalyzed dehydration of 2-propanol. Reactivity and characterization results of Rb/SiO_2 were consistent with the formation of a highly disordered, weakly basic, surface silicate phase that exhibited little activity for alcohol decomposition. The overall rate of acetone formation from 2-propanol correlated with the ranking of support basicity evaluated from the Sanderson intermediate electronegativity principle. These results suggest that strongly basic alkali-containing catalysts should utilize basic carriers to minimize alkali–support interactions that lower base strength.

INTRODUCTION

The oxides of rubidium and cesium have been reported to be "superbases," possessing base strengths with a Hammett basicity function, H_-, exceeding +26 (1). Therefore, it is believed that supported oxides of these alkalis also exhibit strong basicity (2). Sodium was one of the first solid base catalysts studied and was used for the isomerization of olefins (3). More recently, an alumina-supported sodium catalyst was prepared by treatment of γ-alumina with NaOH and Na metal to give a superbasic solid with $H_- > +37$ (4). Other superbasic catalysts have been synthesized by supporting one or more alkali elements on basic supports like MgO and CaO (5–7). These materials are active for the oxidative methylation of acetonitrile with methane to form acrylonitrile (5, 6), dehydrogenation of cumene (7), and isomerization of pentene (7). Lithium-doped magnesia has received much attention due to its ability to abstract hydrogen for the partial oxidation of methane (8–10). Unlike solid superacids, very little work has been done to investigate solid superbases, despite their potential use in many industrial applications which use homogeneous base catalysts (11).

Alkali-modified zeolites, either through ion exchange (12–15) or by decomposition of alkali salts in the zeolite cages (15–19) have recently emerged as interesting new base catalysts. In the case of cesium, zeolites containing excess alkali were found to be much more active than cation-exchanged zeolites (15–19). Temperature-programmed desorption studies indicate that zeolites containing these occluded alkalis have higher base strengths than the ion exchanged materials (17–20). Alkali-loaded zeolites are active for a wide variety of base-catalyzed reactions including 2-propanol dehydrogenation (15), 1-butene isomerization (17–19), and side-chain alkylation of toluene with methanol (16, 21).

The nature of the active surface species is important to the understanding of base catalysis on a molecular level. Recent work with occluded alkali salts in zeolites suggests that, after activation, alkali oxide species are responsible for increased base activity (19, 20, 22). However, the structural complexity of the material obscures the interpretation. The local structure around alkali metal ions on surfaces has not received much attention in the literature. Ternary SiO_2–Cs_2O–Rb_2O glasses have been studied by X-ray absorption at the Cs L_{III} and Rb *K* edges (23). The EXAFS results show changes in the cation environment as a function of composition (23). X-ray absorption studies have also been done at the Rb *K* edge of Rb-promoted ammonia synthesis catalysts under reaction conditions (24). However, to the best of our knowledge, no systematic investigations have been completed in which the local structure around the supported alkali has been related to catalytic activity.

In this paper we examine how rubidium ions interact with a variety of supports in order to gain an understanding

[1] To whom correspondence should be addressed.

0021-9517/97 $25.00

of their effect on base catalysis. X-ray absorption spectroscopy at the rubidium *K* edge, stepwise temperature-programmed desorption (STPD) of CO_2, and Fourier transform infrared (FT-IR) spectroscopy are used to characterize these materials. Even though the mechanism is complicated, decomposition of 2-propanol is frequently used as a test reaction since propene is predominantly formed on acidic oxides and acetone is predominantly formed on basic oxides (2, 25–27).

EXPERIMENTAL METHODS

Synthesis of Rubidium-Modified Catalysts

Several common rubidium precursors, acetate, nitrate, and hydroxide, could be used to synthesize supported catalyst samples. Thermogravimetric analysis indicated that rubidium acetate decomposed in flowing helium at temperatures less than 773 K, which is advantageous for catalyst synthesis. Rubidium nitrate, however, decomposed at higher temperatures. Rubidium hydroxide was avoided due to the extreme basicity of its aqueous solution, which may alter the support surfaces. Therefore, catalysts consisting of about 5 wt% supported rubidium were prepared by incipient wetness impregnation of the appropriate carrier with a solution of rubidium acetate (Aldrich 99.8+%). Magnesia was obtained from the decomposition of magnesium hydroxide (Aldrich 95%) at 873 K for 2 h according to the synthesis method of Aramendia *et al*. (28) and then impregnated with the rubidium precursor. Titania (Degussa P25), γ-alumina (Mager Scientific AP-312), microporous carbon (Armak BAC-LC), and fumed silica (Cab–O–Sil M-5) were dried for 2 h in air at 373 K and then cooled to room temperature before impregnation. The resultant powders were dried at 373 K for 18–24 h. Each catalyst was subsequently heated from room temperature to 773 K at a rate of 4 K min^{-1} and treated for 10 h at this temperature in flowing air. The carbon sample was treated in helium instead of air to prevent oxidation of the support. Elemental analysis was performed by Galbraith Laboratories, Knoxville, Tennessee. Dinitrogen adsorption isotherms were collected on a Coulter Omnisorp 100CX instrument after sample outgassing for 10–12 h at 573 K. X-ray diffraction patterns were obtained on a Scintag diffractometer operating with a Cu $K\alpha$ X-ray source at a scanning rate of 1° min^{-1}.

In Situ X-Ray Absorption Spectroscopy

The X-ray absorption spectra were recorded at the Rb *K* edge (15200 eV) on beam line X18B at the National Synchrotron Light Source, Brookhaven National Laboratory (Upton, NY), in the transmission mode of data collection. The storage ring operated with an electron energy of 2.5 GeV with currents ranging from 100 to 300 mA. Higher harmonics in the beam were rejected by detuning the Si(111) monochromator crystals to give 80% of the maximum intensity. The ionization chambers were filled with an Ar/N_2 mixture to optimize sensitivity. Each sample consisted of a self-supporting wafer of catalyst mixed with boron nitride (Alfa) to adjust absorption, which was loaded into an *in situ* cell capable of heating and cooling in a helium atmosphere. In some cases, the effect of 2-propanol (Mallinckrodt) adsorption on the catalyst was tested by bubbling the helium carrier gas through a 2-propanol saturator maintained at 273 K. The EXAFS data were processed with Macintosh versions of the University of Washington analysis programs. Theoretical EXAFS functions were calculated using a DOS version of FEFF version 5.05 (29–32). Rubidium oxide (Aldrich tech. <1% metal impurities), with an average empirical formula of Rb_2O, was compressed with boron nitride between two Kapton windows and used as a reference material for interatomic distance. An average distance of 2.92 Å was assigned to the average Rb–O distance in rubidium oxide as given by the crystal structure determined by Helms *et al*. (33). Curve fitting was performed in the *k*-space region 1.8–6.0 $Å^{-1}$.

CO_2 Stepwise Temperature-Programmed Desorption

Stepwise temperature-programmed desorption of CO_2 was carried out using a TA Instruments TGA 2050 system. A sample was first heated for 2–4 h in flowing helium (BOC Gases, Grade 6) at 773 K to remove surface adsorbates and water. The sample was then allowed to cool to 303 K at which time carbon dioxide (BOC Gases, Spectra-Clean Grade) was introduced at a constant flow rate of about 100 cm^3 min^{-1} for 2 h. Flowing helium was used to purge the system and remove physisorbed CO_2 from the surface. The temperature was then ramped from room temperature to 373 K at a rate of 10 K min^{-1} and maintained at that temperature for 30 min to allow the adsorbate to completely desorb at that temperature. Additional ramping at 10 K min^{-1} and subsequent holding for 30 min at 473, 573, 673, and 773 K were used to obtain the STPD profile.

Fourier Transform Infrared Spectroscopy

In situ FT-IR spectra were collected using a Bio-Rad FTS-60A spectrometer in the transmission mode with a resolution of 4 cm^{-1}. The sample pellet was heated at a rate of 10 K min^{-1} in flowing dinitrogen to 773 K and held at that temperature for 90 min before cooling to 303 K, where a spectrum was recorded. Carbon dioxide was then introduced to the cell for 30 min to allow for adsorption. After purging the cell with dinitrogen for about 1 h another spectrum was recorded.

Decomposition of 2-Propanol

The decomposition of 2-propanol was carried out in a quartz U-tube continuous-flow fixed-bed reactor, with

catalyst supported by a quartz frit. An empty reactor at 593 K showed no conversion to acetone and negligible production of propene. About 0.5 g of size separated (−40/+60 mesh) fresh catalyst were heated at 10 K min^{-1} to 773 K in flowing helium and held at that temperature for 90 min. The catalyst bed was then cooled to 593 K prior to reaction. Reactant 2-propanol, dried over 3 A molecular sieves, was continuously fed in a 1 : 1 molar ratio with the helium carrier gas (35 cm^3 min^{-1} STP). The product composition was determined by gas chromatography on a Hewlett–Packard HP-5890 fitted with an Alltech Carbowax column. The selectivity is defined here as the rate of acetone production divided by the overall rate of 2-propanol consumption. The turnover frequency for acetone formation is based on a site density estimate from the total CO_2 uptake at 303 K.

RESULTS AND DISCUSSION

A summary of the compositions and surface areas of the samples is presented in Table 1. A drastic loss in surface area was observed for the magnesia support after incorporation of rubidium. A severe loss was also observed by Choudhary *et al.* for mixed rubidium and magnesium carbonates heated to 1173 K (34). The other supports showed only moderate changes in surface area. X-ray diffraction patterns for each of the rubidium-modified supports did not indicate the presence of crystalline rubidium compounds. Apparently the rubidium was well dispersed on each of these catalysts.

XANES and EXAFS and the Rb K Edge

X-ray absorption spectroscopy (XANES and EXAFS) at the Rb *K* edge was performed on each of the samples as a function of treatment temperature in flowing helium. During heating from room temperature to 773 K and after cooling to 77 K, the absorption edge for each sample, defined as the first inflection point in the edge, always occurred about 1 eV lower than that observed for the rubidium oxide reference material. This indicated that the local electron density around the rubidium cation varied little during pretreatment of the samples.

The XANES recorded at 77 K after heating to 773 K in helium are reported in Fig. 1a. Whereas the overall edge position and general features are similar for the samples, subtle differences in the region above the edges are evident. The derivatives of the XANES shown in Fig. 1b enhance these differences and illustrate very clearly that the local environment around the rubidium atoms was affected by the nature of the support.

Figure 2 shows higher resolution XANES recorded on beam line X23A2 (NSLS, Brookhaven National Laboratory) for 5 wt% rubidium impregnated on a high surface area MgO (Ube Industries). A similar spectrum has been reported previously for the Mg *K* edge of MgO impregnated onto magnesium exchanged zeolite Y (18). The Rb/MgO sample contained an extra feature in the edge spectrum near the maximum. This feature did not exist on the sample before pretreatment at 773 K in helium. The presence of an additional suboxide species, carbonate (as detected by IR spectroscopy discussed below), or mixed oxide with magnesium may account for this extra feature. In an attempt to determine if oxygen deficiency was the source of the unusual *K* edge shape for Rb/MgO, the sample was heated to 573 K in a dioxygen mixture (20% O_2 in He). However, treatment with dioxygen failed to restore it to its original state. Therefore, the spectra in Figs. 1a and 2b are representative of the activated Rb/MgO sample.

The effects of 2-propanol adsorption and reaction on the XANES of Rb/Carbon and Rb/Al_2O_3 are shown in Fig. 3. The width of the threshold peak in the XANES of Rb/Carbon narrowed after introduction of 2-propanol as seen by a noticeable shift to lower energy of the first local minimum after the absorption edge (see arrows in Fig. 3). Under identical conditions, 2-propanol addition to Rb/Al_2O_3 had little effect on the local structure around rubidium. Apparently the adsorption and reaction of 2-propanol on Rb/Carbon affects the XANES differently than for rubidium supported on alumina. Additional work is needed to understand the form of rubidium on a carbon support since carbons often contain some bound oxygen.

Figure 4 shows the k^3-weighted EXAFS function and the Fourier transform from $k = 1.8$ to 6.0 $Å^{-1}$ of the rubidium oxide standard. Interestingly, only one major peak was observed for rubidium oxide, likely indicating that only the first shell Rb–O interatomic distance is obtainable from the data. Since Rb_2O has an antifluorite structure, rubidium has only 4 nearest neighbor oxygen, 6 rubidium atoms in the second shell, and 12 rubidium atoms in the third shell. The lack of an observable Rb–Rb distance is intriguing.

In order to test the validity of assigning the peak in the Fourier transform of the rubidium oxide standard to Rb–O, theoretical calculations were performed on a model Rb_2O crystallite containing five shells. The theoretical EXAFS

TABLE 1

Rubidium Loading and Surface Areas of Catalysts

Catalyst	Wt% Rb	Surface area (m^2 g^{-1})
MgO	—	75
Rb/MgO	4.60	16
TiO_2	—	57
Rb/TiO_2	4.88	40
Al_2O_3	—	88
Rb/Al_2O_3	4.57	87
Carbon	—	843
Rb/carbon	4.60	752
SiO_2	—	191
Rb/SiO_2	4.42	129

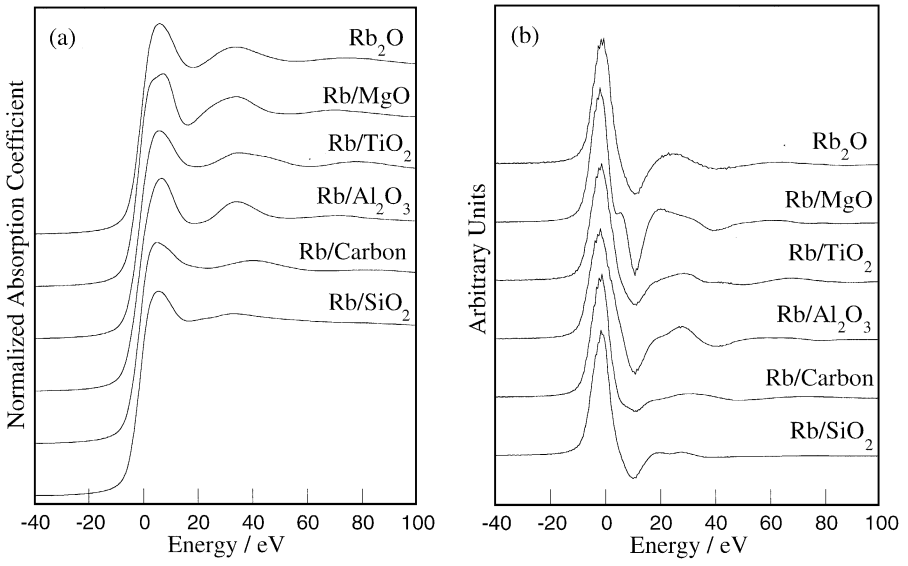

FIG. 1. (a) Rb *K* edge spectra at 77 K for rubidium oxide and rubidium modified supports; (b) derivative of XANES in (a). The zero in energy corresponds to the *K* edge observed for the rubidium oxide standard.

function was generated from FEFF version 5.05 and used to derive the radial structure functions shown in Fig. 5. Over the range of experimentally usable *k*-space for our rubidium oxide standard ($k = 1.8$ to 6.0 $Å^{-1}$), the theoretical analysis shows only one major peak in the RSF, corresponding to the Rb–O distance in the first shell of the antifluorite structure. However, over a larger range in *k*-space ($k = 1.8$ to 19.8 $Å^{-1}$), three distinct Rb–Rb distances are observed. Therefore, we confidently attribute the major peak in the RSF observed experimentally for the rubidium oxide standard to the Rb–O distance. The lack of higher shells in the experimental spectrum could result from large disorder in the sample. For example, the rubidium oxide provided by Aldrich may actually consist of a mixture of rubidium superoxides and suboxides with the overall stoichiometry of Rb_2O.

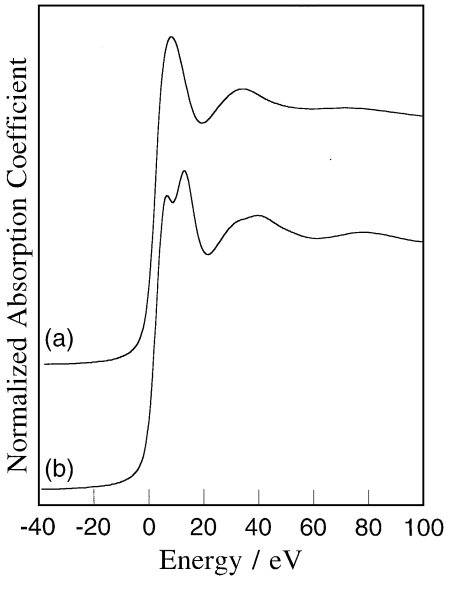

FIG. 2. Rb *K* edge spectra of Rb/MgO(Ube) (a) at room temperature before pretreatment; (b) after high-temperature pretreatment and cooling to 77 K. Spectra recorded on beam line X23A2, NSLS, Brookhaven National Laboratory.

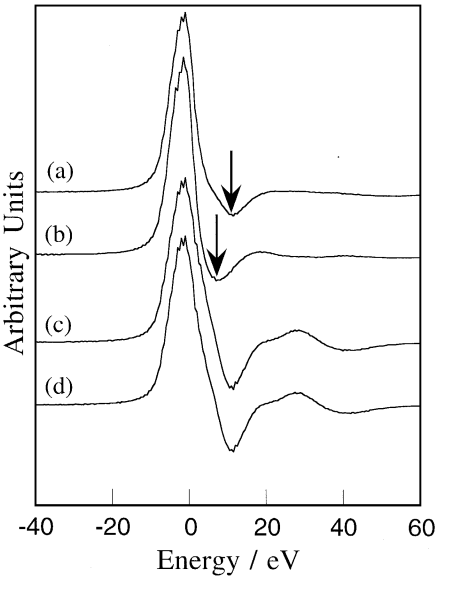

FIG. 3. Effect of 2-propanol adsorption and reaction on the derivative of XANES at 573 K. (a) Rb/carbon in He; (b) Rb/carbon in 2-propanol/He mixture; (c) Rb/Al_2O_3 in He; (d) Rb/Al_2O_3 in 2-propanol/He mixture. Arrows indicate the position of the local minimum of the derivative after the absorption edge.

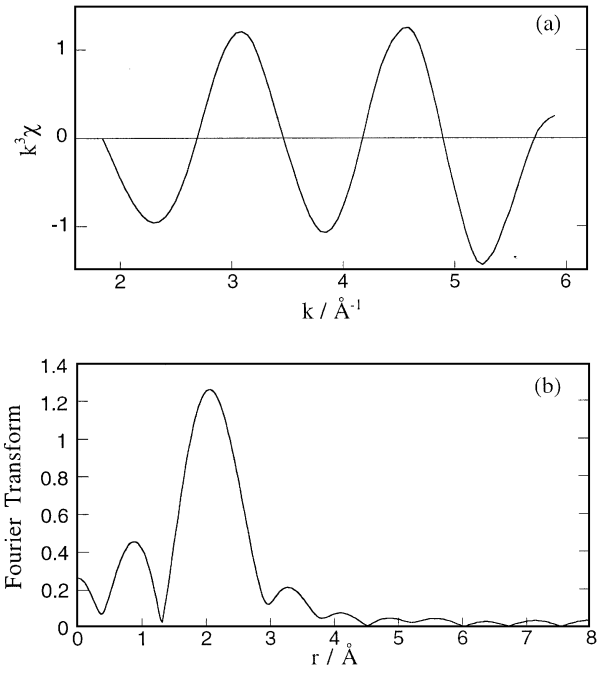

FIG. 4. Rb *K*-edge EXAFS for rubidium oxide at 77 K. (a) $k^3 \cdot \chi(k)$; (b) Fourier transform (radial structure function), not corrected for phase shift.

Due to the lack of accurate information on the atomic potentials, we did not use the theoretical EXAFS function to derive interatomic distances. Instead, we assigned a distance of 2.92 Å to the Rb–O distance in our rubidium oxide standard, based on the crystal structure of pure Rb_2O. Even though this may not be entirely correct due to possible contamination of the oxide standard with other phases, the relative values of the Rb–O distances evaluated for the supported samples are unaffected. Structural information in the vicinity of Rb in each of the modified samples was derived from the Rb *K* edge EXAFS results shown in Fig. 6 through 10. Each of these catalysts showed a strong

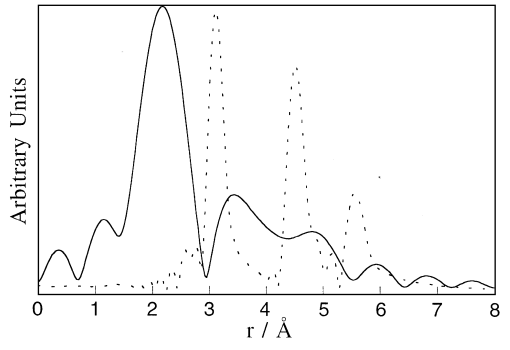

FIG. 5. Normalized Fourier transforms of Rb_2O model cluster obtained from FEFF. Solid line indicates $\Delta k = 1.8$–6.0 Å^{-1}; dotted line indicates $\Delta k = 1.8$–19.8 Å^{-1}.

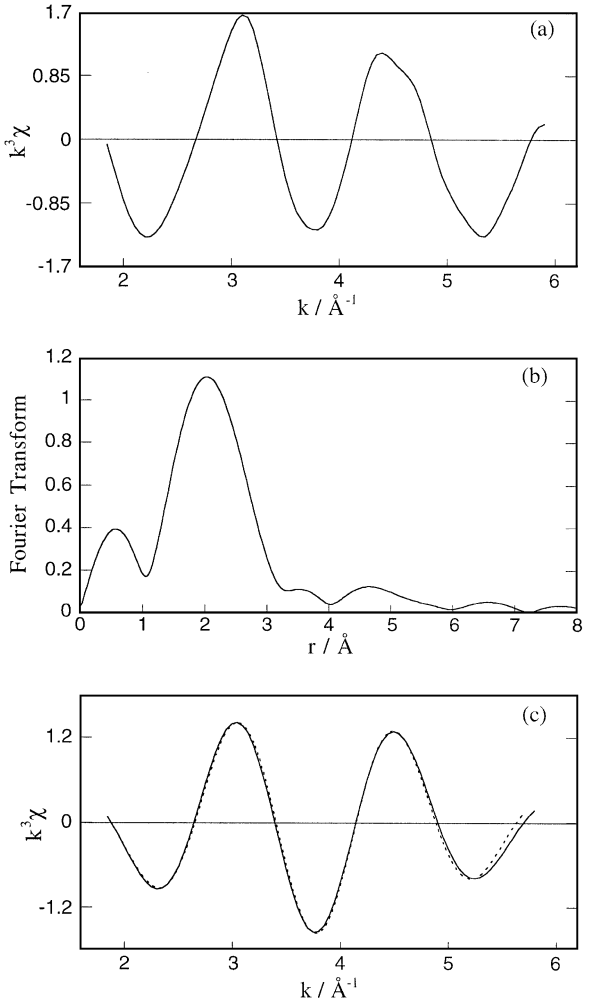

FIG. 6. Rb *K*-edge EXAFS for Rb/MgO at 77 K. (a) $k^3 \cdot \chi(k)$; (b) Fourier transform (radial structure function), not corrected for phase shift; (c) Fourier-filtered EXAFS function and resulting curve fit (dotted line) used to calculate interatomic distance.

characteristic peak attributed to Rb–O except for Rb/SiO_2, which exhibited a much smaller peak, similar in height to the background noise. The loss in Fourier transform intensity for Rb/SiO_2 indicated that a highly disordered surface phase, most likely a rubidium silicate, has been formed.

Since the *k*-space region for analysis was very narrow for these samples (1.8 to 6.0 Å^{-1}), varying the inner potential to minimize the error of the curve fit was not used. The Rb–O distances for the rubidium-loaded materials were evaluated at an inner potential change of zero, which is consistent with the observation that the edge energies were the same in all cases. A summary of the Rb–O distances, as well as the Sanderson intermediate electronegativities of the support and bulk alkali oxide, are shown in Table 2. Sanderson intermediate electronegativity is derived from the concept that, regardless of geometry, each atom in a molecule reaches an intermediate electronegativity (35). The intermediate

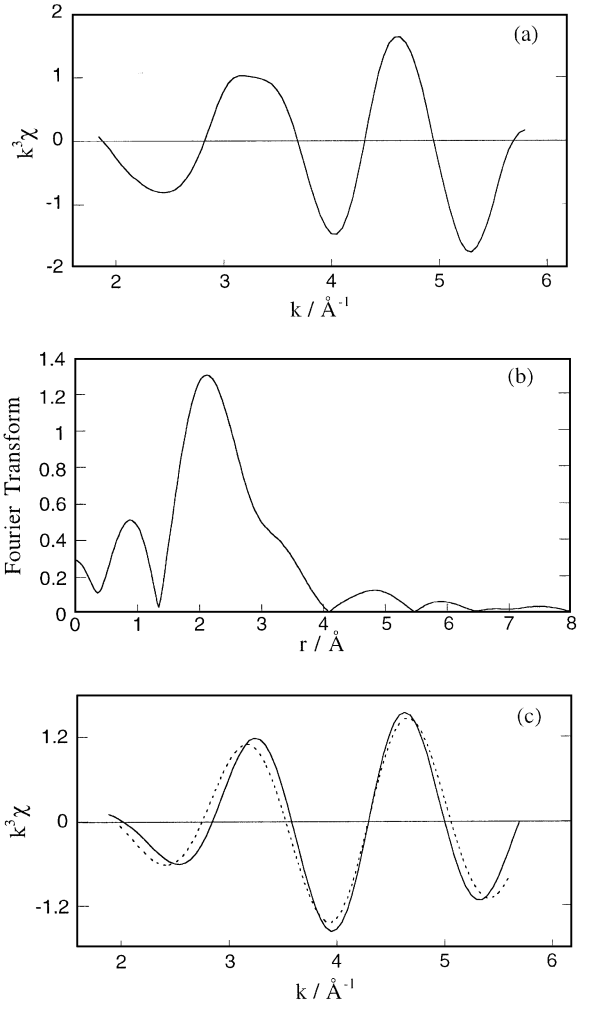

FIG. 7. Rb *K*-edge EXAFS for Rb/TiO_2 at 77 K. (a) $k^3 \cdot \chi(k)$; (b) Fourier transform (radial structure function), not corrected for phase shift; (c) Fourier-filtered EXAFS function and resulting curve fit (dotted line) used to calculate interatomic distance.

electronegativity is therefore calculated from the geometric mean of the electronegativities of the individual atoms (35). Average bulk compositions for each of the carriers were used in calculating these values. In general, as the Sanderson electronegativity of the support increased, and henceforth its acidic nature, the Rb–O distance was found to decrease with the exception of Rb/Al_2O_3. However, we believe that a 5 wt% Rb loading on this γ-alumina sample may have exceeded monolayer surface coverage. Thus, the simple correlation of Rb–O distance with support electronegativity would not apply to this case.

TABLE 2

Rubidium–Oxygen Interatomic Distances for Supported Catalysts at 77 K

Catalyst	Rb–O interatomic distance (Å)	Sanderson intermediate electronegativity of the support
Bulk Rb_2O	2.92	—
Rb/MgO	2.94	2.80
Rb/TiO_2	2.86	3.36
Rb/Al_2O_3	2.91	3.70
Rb/carbon	2.78	3.74
Rb/SiO_2	2.80	4.26

STPD of CO_2 as a Probe for Basicity

The total carbon dioxide uptake at 303 K for the samples is given in Table 3. Each of the supports showed increased adsorption capacity after incorporation of rubidium on the surface. Excess CO_2 adsorbed was determined by subtracting the mass of CO_2 adsorbed on the pure support from that of its Rb-modified counterpart, on both a surface area and a rubidium atom basis. The value of 0.99 for excess CO_2

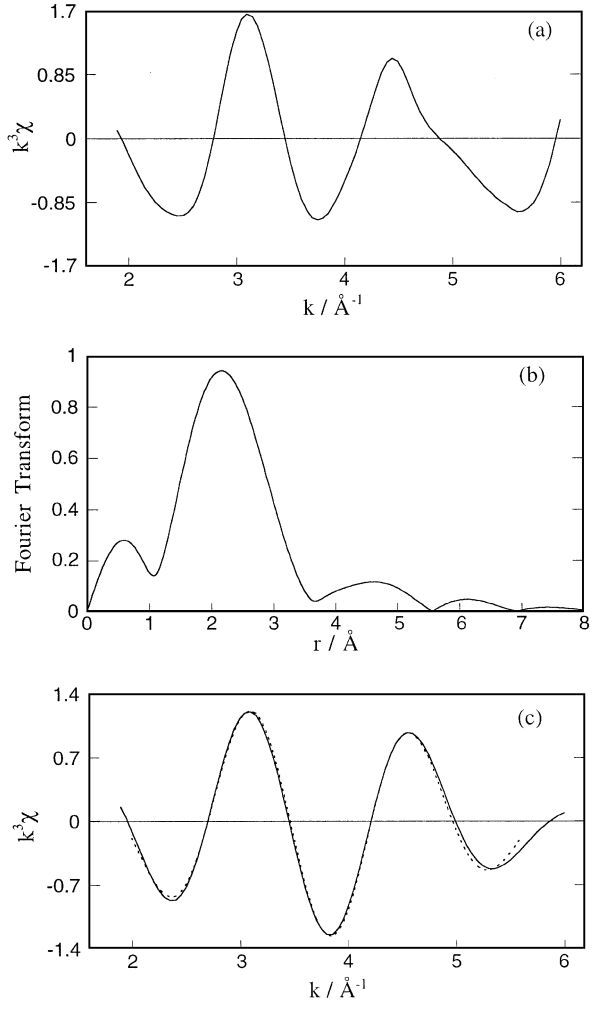

FIG. 8. Rb *K*-edge EXAFS for Rb/Al_2O_3 at 77 K. (a) $k^3 \cdot \chi(k)$; (b) Fourier transform (radial structure function), not corrected for phase shift; (c) Fourier-filtered EXAFS function and resulting curve fit (dotted line) used to calculate interatomic distance.

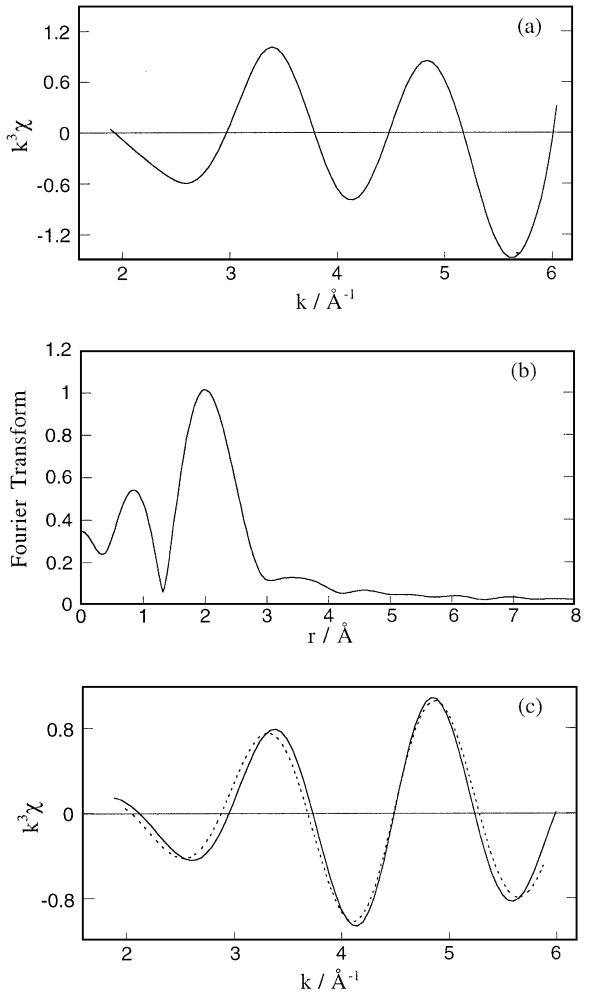

FIG. 9. Rb *K*-edge EXAFS for Rb/carbon at 77 K. (a) $k^3 \cdot \chi(k)$; (b) Fourier transform (radial structure function), not corrected for phase shift; (c) Fourier-filtered EXAFS function and resulting curve fit (dotted line) used to calculate interatomic distance.

adsorbed per Rb on supported carbon showed that the alkali was well dispersed on the carbon and that there was a 1 : 1 stoichiometry between adsorption sites and added rubidium atoms. The other samples showed a smaller increase in adsorption capacity than that of Rb/Carbon, which may be due to different CO_2 adsorption stoichiometry or movement of rubidium into subsurface positions.

Figure 11 shows the results obtained from stepwise temperature-programmed desorption of CO_2 from all samples. For rubidium on titania and alumina, a majority of the new basic adsorption sites were fairly weak, as shown by a large increase in CO_2 desorption at lower temperatures. However, some new stronger base sites were also observed on these samples. Since pure silica and pure carbon adsorbed no CO_2 under our conditions, STPD profiles are not reported. The STPD plots for the rubidium-modified silica and carbon samples indicated the formation of new basic adsorption sites, most of them being fairly weak. In contrast, an increase in strong base sites on Rb/MgO was observed. The incorporation of Rb on the MgO surface, despite drastically reducing the available surface area, allowed for stronger base sites to be produced per unit surface area than on the other supports.

FT-IR Spectroscopy of Chemisorbed Carbon Dioxide

Infrared spectra for each of the rubidium-modified catalysts were obtained after heating under pretreatment conditions in dinitrogen. Spectra could not be obtained for carbon and Rb/carbon due to the high absorptivity of the support. Rubidium acetate bands were not observed on any of the supports studied, indicating that 773 K is adequate for the decomposition of the impregnated precursor. Also, the spectrum for each rubidium-modified catalyst did not show the presence of bulk rubidium carbonate. Evidently, bulk phase Rb_2CO_3 was not formed upon calcination at

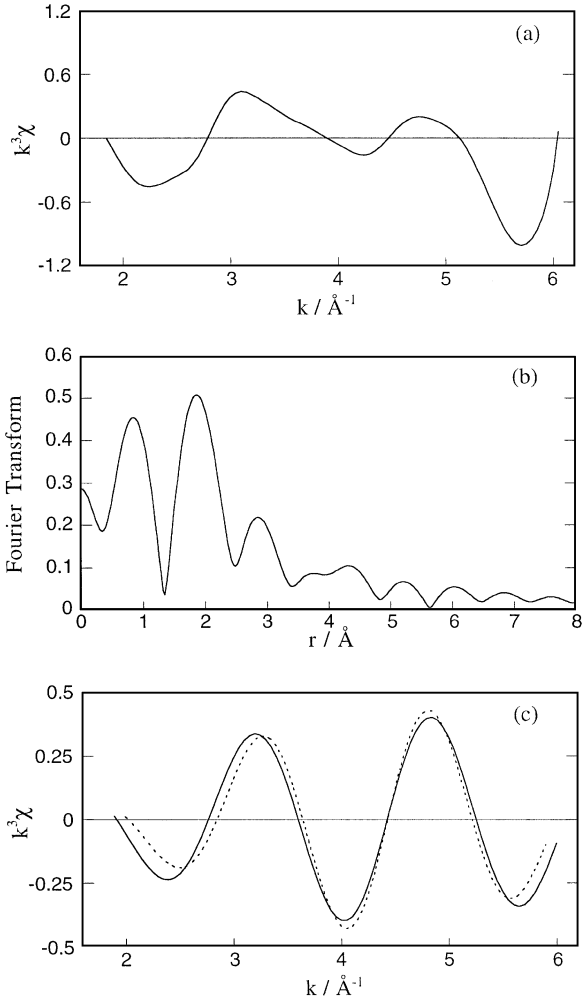

FIG. 10. Rb *K*-edge EXAFS for Rb/SiO_2 at 77 K. (a) $k^3 \cdot \chi(k)$; (b) Fourier transform (radial structure function), not corrected for phase shift; (c) Fourier-filtered EXAFS function and resulting curve fit (dotted line) used to calculate interatomic distance.

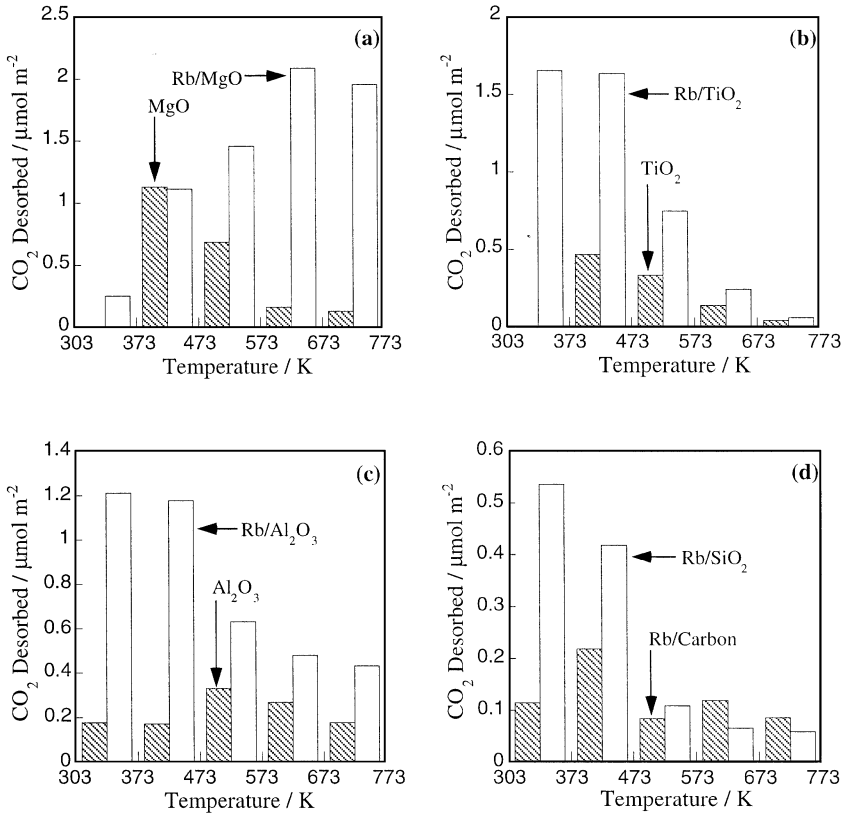

FIG. 11. Stepwise temperature-programmed desorption of CO_2 from (a) MgO and Rb/MgO; (b) TiO_2 and Rb/TiO_2; (c) Al_2O_3 and Rb/Al_2O_3; and (d) Rb/carbon and Rb/SiO_2. Carbon and SiO_2 did not adsorb CO_2 under our experimental conditions.

773 K for any of the catalyst samples. It appears that the Rb precursor interacted differently with each support and did not decompose to form the same surface species on each carrier.

The IR absorption spectra for MgO, before and after incorporation of Rb, are shown in Fig. 12. The spectrum for bulk phase Rb_2CO_3 (Aldrich 99%) is shown for comparison purposes. Pure magnesia did not exhibit any strong carbonate bands after pretreatment in dinitrogen at 773 K. However, a band at 1396 cm^{-1} and a shoulder at about 1500 cm^{-1} for Rb-loaded magnesia clearly indicated the presence of carbonates on the sample, even after pretreatment at 773 K. Higher temperatures are needed to decompose those carbonates and expose very strong base sites. Chemisorption of CO_2 on Rb/MgO at 303 K caused little change in the IR spectrum; the only new carbonate

TABLE 3

Carbon Dioxide Adsorption Capacities at 303 K

Catalyst	CO_2 adsorbed (μmol m^{-2})	Excess CO_2 adsorbed (μmol m^{-2})	Excess CO_2 adsorbed per mole of Rb (mol (mol Rb)$^{-1}$)
MgO	2.67	—	—
Rb/MgO	7.16	4.49	0.13
TiO_2	0.82	—	—
Rb/TiO_2	4.22	3.40	0.24
Al_2O_3	0.90	—	—
Rb/Al_2O_3	4.55	3.65	0.59
Carbon	0.00	—	—
Rb/carbon	0.71	0.71	0.99
SiO_2	0.00	—	—
Rb/SiO_2	1.16	1.16	0.29

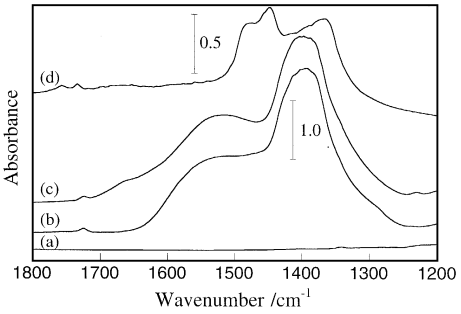

FIG. 12. FT-IR spectra of the carbonate region for (a) MgO at 303 K after pretreatment; (b)Rb/MgO at 303 K after pretreatment; (c) sample in (b) after CO_2 adsorption and dinitrogen purge; (d) Rb_2CO_3 in KBr at room temperature.

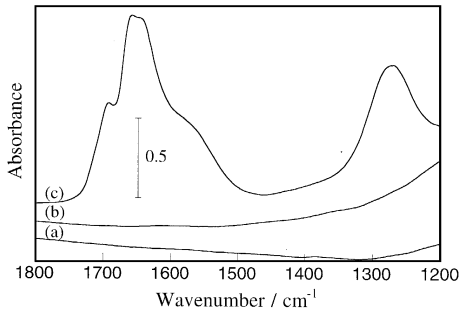

FIG. 13. FT-IR spectra of the carbonate region for (a) TiO_2 at 303 K after pretreatment; (b) Rb/TiO_2 at 303 K after pretreatment; (c) sample in (b) after CO_2 adsorption and dinitrogen purge.

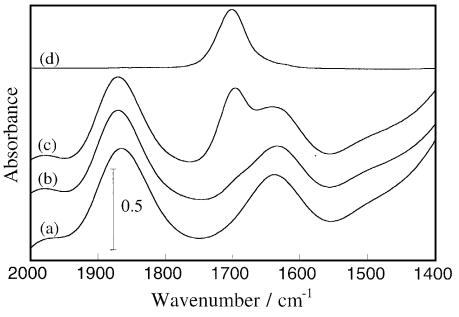

FIG. 15. FT-IR spectra of the carbonate region for (a) SiO_2 at 303 K after pretreatment; (b) Rb/SiO_2 at 303 K after pretreatment; (c) sample in (b) after CO_2 adsorption and dinitrogen purge; (d) spectrum (c)−spectrum (b).

absorption peak occurred at 1512 cm^{-1}. The remaining bands, originally observed for the Rb-modified sample, did not change with CO_2 adsorption.

As seen in Fig. 13, both TiO_2 and Rb/TiO_2 did not reveal any carbonate bands in their spectra after pretreatment in dinitrogen at 773 K. However, carbon dioxide adsorption on rubidium-modified titania profoundly affected the carbonate region of the spectrum. Three distinct bands appeared between 1600 and 1700 cm^{-1} at 1692, 1657, and 1647 cm^{-1} and one low wavenumber band was found at 1269 cm^{-1}. The shoulders seen at about 1570 and 1330 cm^{-1} were features also observed after CO_2 adsorption on the pure support. The IR absorption spectra for Al_2O_3, before and after incorporation of Rb, are shown in Fig. 14. Chemisorption of CO_2 on Rb/Al_2O_3 at 303 K caused absorption bands at 1640, 1605, and 1319 cm^{-1}. The band at 1640 cm^{-1} and the shoulder at 1235 cm^{-1} were features also seen after chemisorption of carbon dioxide on pure alumina. At least seven basic types of surface species can be formed by chemisorption of CO_2 onto metal oxides (36). These consist of carbonate (free carbonate, unidentate, bidentate, and bridged), bicarbonate, carboxylate, and formate (36, 37). Each of these have characteristic vibrational stretching frequencies in the range from 1200 to 1850 cm^{-1}. Since bidentate carbonate shows characteristic IR bands from 1600 to 1670 cm^{-1} and 1280 to 1310 cm^{-1} (37), and rubidium-modified titania and alumina both exhibit bands near these regions, bidentate carbonate may be the surface species observed on these materials after CO_2 adsorption. After exposure to carbon dioxide, heating both Rb/TiO_2 and Rb/Al_2O_3 while purging in dinitrogen resulted in a majority of the surface carbonate bands disappearing by 573 K, which is consistent with observations from CO_2 STPD.

The IR absorption spectra for SiO_2, before and after incorporation of Rb, are shown in Fig. 15. The Rb/SiO_2 sample exhibited absorption bands characteristic of pure SiO_2 in the carbonate region of its spectrum after pretreatment in dinitrogen at 773 K. Chemisorption of carbon dioxide on Rb/SiO_2 at 303 K produced a carbonate band at 1693 cm^{-1}, which can be seen in Fig. 15d. The observed carbonate band was consistent with bidentate carbonate, but the accompanying low wavenumber band was obscured due to high absorption of silica below 1400 cm^{-1}. The carbonate peak disappeared after heating of the catalyst *in situ* to 373 K, confirming the very weak basicity of the surface. Figure 16 shows the effect of rubidium incorporation on the hydroxyl region of the IR spectrum. The significant decrease in the OH band after incorporation of rubidium is consistent with ion exchange of surface protons by rubidium cations and/or the formation of a surface rubidium silicate phase.

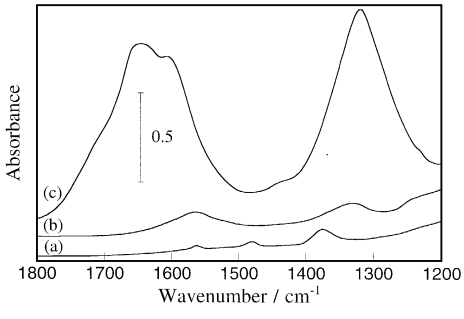

FIG. 14. FT-IR spectra of the carbonate region for (a) Al_2O_3 at 303 K after pretreatment; (b) Rb/Al_2O_3 at 303 K after pretreatment; (c) sample in (b) after CO_2 adsorption and dinitrogen purge.

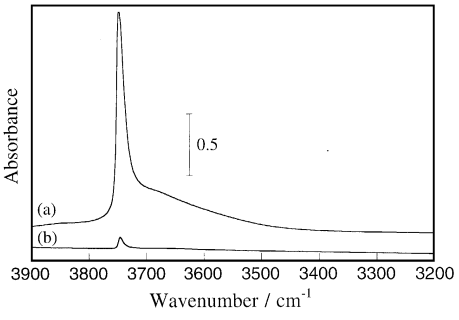

FIG. 16. FT-IR spectra of the hydroxyl region for (a) SiO_2 at 303 K after pretreatment; (b) Rb/SiO_2 at 303 K after pretreatment.

TABLE 4

Decomposition of 2-Propanol at 593 K

Catalyst	Rate (10^{-9} mol m^{-2} s^{-1})	Turnover frequency[a] (10^{-3} s^{-1})	Selectivity to acetone (%)
MgO	1.91	0.66	93.2
Rb/MgO	26.6	3.58	96.5
TiO_2	Very high[b]	—	0.8
Rb/TiO_2	10.3	1.63	66.9
Al_2O_3	Very high[c]	—	0.2
Rb/Al_2O_3	3.80	0.64	76.7
Carbon	0.46	—	32.7
Rb/carbon	0.89	0.96	76.5
SiO_2	19.4	—	1.3
Rb/SiO_2	0.56	0.07	13.8

[a] Rate of acetone formation normalized by the site density counted by CO_2 adsorption at 303 K.
[b] 70% conversion under reaction conditions.
[c] 100% conversion under reaction conditions.

Results from both X-ray and infrared spectroscopies indicate that the local environment around the rubidium atoms is strongly dependent on the nature of the support.

Decomposition of 2-Propanol

Reactivity results for the decomposition of 2-propanol at 593 K are summarized in Table 4. The steady-state rate was reported after 2 h of reaction. Turnover frequencies are not included for pure carbon and pure silica due to their lack of CO_2 adsorption at 303 K. For each of the rubidium-modified catalysts, conversion of 2-propanol was less than 5% and rates were calculated assuming differential conversion. However, decomposition of 2-propanol over pure Al_2O_3 and pure TiO_2 occurred with very high overall conversion (100 and 70%, respectively), even though conditions were identical to those used for the study of Rb-modified supports. Previous studies in our lab showed that 2-propanol decomposes with high selectivity to propene over alumina at low conversion (38, 39). Likewise, temperature-programmed reaction of 2-propanol adsorbed on titania revealed that propene is produced without any formation of acetone (40). These observations are consistent with the low acetone selectivities reported for alumina and titania in this study. Due to the high conversions for these two samples, rates of reaction are not reported in Table 4.

Pure magnesia, a basic oxide, was highly selective to acetone formation. Rubidium incorporation onto magnesia increased the turnover frequency by a factor of 5. In addition, the rate of acetone formation, normalized to total surface area, increased by an order of magnitude with rubidium loading. Incorporation of the alkali increased both the CO_2 adsorption capacity and the rate of 2-propanol dehydrogenation. Even though carbonates were detected on the magnesia sample, the rubidium-modified material was highly active and selective for alcohol dehydrogenation.

Incorporation of rubidium on the surfaces of alumina and titania neutralized a majority of the acid sites responsible for the high conversion of 2-propanol to propene over the unmodified supports, resulting in higher selectivity to the base-catalyzed acetone product. An increase in the amount of base sites, as seen by CO_2 stepwise temperature-programmed desorption, also helped to increase the selectivity for this reaction.

Pure carbon and pure silica, despite having no CO_2 adsorption capacity under our conditions, exhibited some catalytic activity. However, their activity for acetone formation was less than the other catalysts in this study. The increase in selectivity for rubidium-modified silica was due to neutralization of surface acid sites and by formation of new basic sites.

The areal rate for Rb/carbon after 2 h was found to be double that of pure carbon. With increasing time on stream, however, the Rb/carbon sample significantly deactivated as the reaction was probed at temperatures up to 633 K. After 12 h, rates and selectivities were found to be almost identical to that of pure carbon. The rubidium species on carbon lost its activity as a surface modifier under reaction conditions; thus the high rubidium dispersion was not effective for catalysis under these conditions.

The areal rates observed for each of the rubidium-modified carriers shows that a decrease in both the overall and acetone rates of formation is observed for increasing support Sanderson intermediate electronegativity, and thus acidity. The trend with support acidity is also roughly followed by the turnover frequency for acetone formation, except for the Rb/carbon case.

This study indicates that effective heterogeneous strong base catalysts should be prepared from alkali incorporation onto basic solids in order to prevent significant alkali–support interactions which form weak base sites. However, as demonstrated with Rb/MgO, decomposition of surface carbonates on strongly basic materials will require higher temperatures than those used in this work.

CONCLUSIONS

Incorporation of alkali ions onto various supports not only eliminated some of the surface acid sites but also created new basic sites. Results from XANES, EXAFS, and IR spectroscopy of supported Rb catalysts confirmed that the environment around the alkali is significantly affected by the support composition. The basicity of the supports used in this work, ranked in the following order based on their intermediate Sanderson electronegativity values, is calculated as magnesia > titania > alumina > carbon > silica. Interestingly, the strongest basic sites formed by incorporation of Rb were found on Rb/MgO, which contained

significant carbonate species after heating to 773 K. Carbonates were not present on the other heat-treated Rb catalysts. The least basic support, silica, is thought to react with Rb to form a highly disordered, weakly basic surface silicate. Rates of 2-propanol decomposition to acetone over the supported Rb catalysts followed the same trend as the basicity ranking of the pure supports. Evidently, the strong interaction of the alkali with the support surface moderates the strength of the newly formed basic sites.

ACKNOWLEDGMENTS

This work was supported by the Department of Energy (Basic Energy Sciences, Grant DEFG05-95ER14549). Research was carried out in part at the National Synchrotron Light Source, Brookhaven National Laboratory, which is supported by the U.S. Department of Energy, Division of Materials-Sciences and Division of Chemical Sciences (DOE Contract DE-AC02-76CH00016).

REFERENCES

1. Tsuchiya, S., Takase, S., and Imamura, H., *Chem. Lett.* 661 (1984).
2. Tanabe, K., Misono, M., Ono, Y., and Hattori, H., "New Solid Acids and Bases," Kodansha, Tokyo, 1989.
3. Pines, H., Vesely, J. A., and Ipatieff, V. N., *J. Am. Chem. Soc.* **77**, 347 (1955).
4. Suzukamo, G., Fukao, M., and Minobe, M., *Chem. Lett.* 585 (1987).
5. Ruckenstein, E., and Khan, A. Z., *J. Catal.* **141**, 628 (1993).
6. Ruckenstein, E., and Khan, A. Z., *J. Chem. Soc., Chem. Commun.* 1290 (1993).
7. Kijenski, J., and Malinowski, S., *J. Chem. Soc., Trans. 1* **74**, 250 (1978).
8. Ito, T., and Lunsford, J. H., *Nature* **314**, 721 (1985).
9. Driscoll, D. J., Martir, W., Wang, J.-X., and Lunsford, J. H., *J. Am. Chem. Soc.* **107**, 58 (1985).
10. Ito, T., Wang, J.-X., Lin, C.-H., and Lunsford, J. H., *J. Am. Chem. Soc.* **107**, 5062 (1985).
11. Hattori, H., *Chem. Rev.* **95**, 537 (1995).
12. Yashima, T., Sato, K., Hayasaka, T., and Hara, N., *J. Catal.* **26**, 303 (1972).
13. Onaka, M., Ishikawa, K., and Izumi, Y., *Chem. Lett.* 1783 (1982).
14. Corma, A., Fornes, V., Martin-Aranda, R. M., Garcia, H., and Primo, J., *Appl. Catal.* **59**, 237 (1990).
15. Hathaway, P. E., and Davis, M. E., *J. Catal.* **116**, 263 (1989).
16. Hathaway, P. E., and Davis, M. E., *J. Catal.* **119**, 497 (1989).
17. Tsuji, H., Yagi, F., Hattori, H., and Kita, H., *in* "Proceedings, 10th International Congress on Catalysis, Budapest, 1992" (L. Guczi, F. Solymosi, and P. Tetenyi, Eds.), Akadémiai, Kiadó, Budapest, 1993.
18. Tsuji, H., Yagi, F., and Hattori, H., *Chem. Lett.* 1881 (1991).
19. Kim, J. C., Li, H.-X., Chen, C.-Y., and Davis, M. E., *Microporous Mater.* **2**, 413 (1994).
20. Lasperas, M., Cambon, H., Brunel, D., Rodriguez, I., and Geneste, P., *Microporous Mater.* **7**, 61 (1996).
21. Wieland, W. S., Davis, R. J., and Garces, J. M., *Catal. Today* **28**, 443 (1996).
22. Hathaway, P. E., and Davis, M. E., *J. Catal.* **116**, 279 (1989).
23. Landron, C., Dexpert, H., Douy, A., and Coutures, J. P., *J. Chim. Phys.* **56**, 1587 (1989).
24. Clausen, B. S., Niemann, W., and Topsoe, H., *Phys. B* **158**, 160 (1989).
25. Ai, M., *Bull. Chem. Soc. Jpn.* **50**, 2579 (1977).
26. Noller, H., and Ritter, G., *J. Chem. Soc., Faraday Trans. 1* **80**, 275 (1984).
27. Gervasini, A., and Auroux, A., *J. Catal.* **131**, 190 (1991).
28. Aramendia, M., Borau, V., Jimez, C., Marinas, J., Porras, A., and Urbano, F., *React. Kinet. Catal. Lett.* **53**, 397 (1994).
29. Rehr, J. J., Zabinsky, S. I., and Albers, R. C., *Phys. Rev. Lett.* **69**, 3397 (1992).
30. Rehr, J. J., and Albers, R. C., *Phys, Rev. B* **41**, 8139 (1990).
31. Rehr, J. J., Mustre de Leon, J., Zabinsky, S. I., and Albers, R. C., *J. Am. Chem. Soc.* **113**, 5135 (1991).
32. Mustre de Leon, J., Rehr, J. J., Zabinsky, S. I., and Albers, R. C., *Phys. Rev. B* **44**, 4146 (1991).
33. Helms, A., and Klemm, W., *Z. Anorg. Allg. Chem.* **242**, 33 (1939).
34. Choudhary, V. R., Pataskar, S. G., Pandit, M. Y., and Gunjikar, V. G., *Thermochim. Acta.* **180**, 69 (1991).
35. Sanderson, R. T., "Chemical Bonds and Bond Energy," Academic Press, New York, 1976.
36. Busca, G., and Lorenzelli, V., *Mater. Chem.* **7**, 89 (1982).
37. Kiselev, V. F., and Krylov, O. V., "Adsorption and Catalysis on Transition Metals and Their Oxides" (G. Ertl and R. Gomer, Eds.), Springer Series in Surface Sciences. Springer-Verlag, Berlin (1989).
38. McKenzie, A. L., Fishel, C. T., and Davis, R. J., *J. Catal.* **138**, 547 (1992).
39. Fishel, C. T., and Davis, R. J., *Catal. Lett.* **25**, 87 (1994).
40. Liu, Z., Tabora, J., and Davis, R. J., *J. Catal.* **149**, 117 (1994).